# System Design for Geosynchronous Synthetic Aperture Radar Missions

Stephen Hobbs, Cathryn Mitchell, Biagio Forte, Rachel Holley, *Member, IEEE*, Boris Snapir, and Philip Whittaker

***Abstract*—Geosynchronous synthetic aperture radar (GEO SAR) has been studied for several decades but has not yet been implemented. This paper provides an overview of mission design, describing significant constraints (atmosphere, orbit, temporal stability of the surface and atmosphere, measurement physics, and radar performance) and then uses these to propose an approach to initial system design. The methodology encompasses all GEO SAR mission concepts proposed to date. Important classifications of missions are: 1) those that require atmospheric phase compensation to achieve their design spatial resolution; and 2) those that achieve full spatial resolution without phase compensation. Means of estimating the atmospheric phase screen are noted, including a novel measurement of the mean rate of change of the atmospheric phase delay, which GEO SAR enables. Candidate mission concepts are described. It seems likely that GEO SAR will be feasible in a wide range of situations, although extreme weather and unstable surfaces (e.g., water, tall vegetation) prevent 100% coverage. GEO SAR offers an exciting imaging capability that powerfully complements existing systems.**

***Index Terms*—Atmosphere, geosynchronous (GEO), mission, synthetic aperture radar (SAR), system.**

## I. Introduction

GEOSYNCHRONOUS synthetic aperture radar (GEO SAR) offers significant advantages compared with low-Earth-orbit (LEO) systems. The concept raises significant technical challenges too. This paper provides an overview of mission concepts and identifies the principal system design choices and constraints.

Tomiyasu and Pacelli [1] first discussed a GEO SAR mission. The proposed orbit inclination was 50° to provide coverage of North and South America, the antenna diameter was 15–30 m and a mean transmitter RF power of 0.1–1 kW gave a spatial resolution of 100 m. Madsen *et al.* [2] adapted the concept and improved the ground resolution to 10–45 m (varying with position) at the cost of increased power (20 kW electrical), using L-band. Applications included disaster response, tectonic mapping, and soil moisture. Similar studies from the United States include [3] and [4]. All these studies recognize the much improved temporal sampling, which is possible from GEO compared with LEO, and the new measurement opportunities this creates.

In Europe, one of the first published GEO SAR concepts was by Prati *et al.* [5] in 1998. They described a bistatic passive radar reusing L-band broadcast signals. Such a system could achieve 120-m spatial resolution using an antenna with a diameter 4.8 m. The orbit inclination is small (satellite motion of only 25 km from the geostationary position is assumed). However, a long integration time of up to 8 h is required to form a satisfactory image. Imaging effects of clutter and partially stable targets, as well as measuring the atmospheric phase screen (APS) are noted. Research on other GEO SAR concepts (mainly conventional monostatic) has continued with contributions from Cranfield [6]–[8], Milan [9]–[11], and Barcelona [12], [13] in particular. These recent studies have made significant contributions in the areas of system design and APS estimation/phase compensation. For the low inclination orbits and modest antenna sizes, which these authors have assumed, integration times are relatively long, and thus, atmospheric phase compensation is needed. There has been particular interest again in applications for short repeat period interferometry related to geohazards.

A third and very active GEO SAR research community exists in China. The main concepts discussed relate to systems using high-inclination orbits with large antennas and high power to achieve fine resolution. These systems provide excellent coverage of continental areas, such as the Chinese mainland. Particular attention has been given to methods of adapting frequency-domain focusing algorithms to cope with the curved trajectories typical of GEO SAR, e.g., [14]–[17]. Other topics studied include aspects of system design [18] and atmospheric perturbations [19]. Reference [20] described two indicative mission concepts currently being evaluated, with inclinations of 16° and 53°.

GEO implies longer integration times $t_{\mathrm{int}}$ than for LEO. The atmosphere may change significantly during $t_{\mathrm{int}}$, affecting the phase of the received signals. SAR depends on accurate phase compensation, and thus, an important classifications of types of missions are: a) those that require atmospheric phase compensation to achieve their design spatial resolution; and b) those that achieve full spatial resolution without phase compensation. The U.S. and Chinese missions tend to fall into the second group, and the European ones into the first. This bifurcation of concepts is discussed below.

We focus here on the engineering design of monostatic concepts. Bi- and multistatic concepts are also under consideration [11]. Much of the system design is common to all types or can

Manuscript received November 25, 2013; revised January 28, 2014; accepted April 2, 2014. Date of publication May 8, 2014; date of current version June 12, 2014. This work was supported in part by the U.K.'s Centre for Earth Observation Instrumentation and in part by the Engineering and Physical Sciences Research Council under Grant EP/H003304/1.

S. Hobbs and B. Snapir are with the Space Research Centre, Cranfield University, Bedford MK43 0AL, U.K. (e-mail: s.e.hobbs@cranfield.ac.uk).

C. Mitchell and B. Forte are with the University of Bath, Bath BA2 7AY, U.K.

R. Holley is with NPA Satellite Mapping, Kent TN8 6SR, U.K.

P. Whittaker is with Surrey Satellite Technology Ltd., Guildford GU2 7YE, U.K.

Color versions of one or more of the figures in this paper are available online at http://ieeexplore.ieee.org.

Digital Object Identifier 10.1109/TGRS.2014.2318171

TABLE I
TYPICAL TID PARAMETER VALUES FOR MID-LATITUDE REGIONS. THE TEC VALUES ARE FOR A ONE-WAY VERTICAL PATH THROUGH THE ATMOSPHERE AND THE MEAN HEIGHT OF THE DISTURBANCE IS 250 km; BOTH LARGE AND MEDIUM TIDS TEND TO TRAVEL FROM THE POLE TO THE EQUATOR

| Type | Solar cycle | Wavelength km | Velocity m $s^{-1}$ | Amplitude % | Mean TEC TECU | Comments |
|---|---|---|---|---|---|---|
| Medium | min | 300 | 250 | 5–15 | 20 | Max. amplitude seen is 40% over Japan; most common in winter. |
| | max | 300 | 250 | 10 | 100 | |
| Large | min | 1000 | 750 | 5–20 | 20 | |
| | max | 1000 | 750 | 5–20 | 100 | Large waves possible in superstorms ($<$ 5% of solar cycle) |

be extended in obvious ways. We do not discuss polarimetry, but note that the BIOMASS P-band mission, which is likely to suffer more severe Faraday polarization rotations than any GEO SAR concept so far considered, expects to provide useful polarimetric data.

The aims of the initial system design outlined here are to assess the feasibility of a mission concept and to identify the main technical challenges. System design is iterative: later iterations include the realism needed to improve the design starting with the most significant challenges. It is more important that the initial system design be complete than that it incorporates comprehensive detail from the outset.

The paper has two main sections. Section II reviews the main physical constraints on GEO SAR system design. Section III proposes an outline system design methodology, which addresses these constraints and identifies feasible sets of system parameters. Example designs are shown and we briefly discuss the information available for estimating the APS. A short discussion closes the paper.

## II. MISSION CONSTRAINTS

Before discussing system design, it is important to understand relevant constraints. The factors discussed here are:

- atmosphere;
- orbit;
- SAR image focusing;
- signal averaging in time and space;
- radar performance.

### A. Atmosphere

Refractive index fluctuations in the atmosphere affect the signal phase. This is mainly due to changes in the ionospheric electron content and the tropospheric humidity. System design is an iterative process, and thus, initial models of atmospheric perturbations are usually simple. For this initial design, we start with simple, even simplistic, representations of atmospheric perturbations. As the system design develops, increasingly sophisticated models are used to assess system performance in a wider range of conditions and to resolve design challenges. Useful overviews of the effects of the atmosphere on SAR imaging from space are provided by [21]–[23].

*1) Ionosphere:* Ionization of Earth's atmosphere (from heights of 50 km to over 500 km) by short wavelength solar radiation changes its refractive index enough to affect radio propagation. Changes in the level of this ionization in space and time affect radar imaging from the Earth orbit. Ionization is measured in terms of the free electron density (total electron content [TEC]), expressed generally as column density, i.e., number of electrons per unit area of the Earth's surface for a vertical column to the "top" of the atmosphere. The column density is usually expressed in TEC units (TECUs), i.e., units of $10^{16}$ electrons per square meter. Ionospheric plasma density and its variability increase near the peaks of the 11-year solar cycle.

The ionosphere has a regular diurnal pattern of behavior, driven by the Sun, in addition to which it varies with space and time on a wide range of scales. The most active areas are near the equator from sunset to midnight and at high latitudes. In mid-latitudes, where much GEO SAR imaging is likely to be done, some of the most important features are traveling ionospheric disturbances (TIDs). Reference [24] reported observations of medium-scale TIDs over Europe, where occurrence is below 15% for most of the year, but in winter around midday (UT), the rate can reach 70%; there are also peaks up to 45% during nighttime. Reference [25] reported that typical TID amplitudes are 0.2–1 TECU (peak-to-peak, solar minimum) to 1–2 TECU (solar maximum). Large-scale TIDs are much rarer although amplitudes well over 10 TECU are sometimes seen. Periods range from 0.5 to 3 h, with a typical value of 1.5 h. Other observations of medium-scale TIDs [26] give velocities of 150–250 m $\cdot$ $s^{-1}$ and wavelengths of 100–300 km. Although published values differ, representative TID speeds, amplitudes, and wavelengths are given in Table I. A simple approach is to model these as waves propagating from the poles to the equator: this is used here.

TEC values can be converted to an equivalent range error using (1) [27, p. 211], with $K = -40.28$ $m^3 \cdot s^{-2}$. Increasing TEC reduces the path phase delay, and the process is dispersive, i.e., the effect varies with frequency. Thus

$$\delta = \frac{K}{f^2}\,\mathrm{TEC}. \tag{1}$$

*2) Troposphere:* Most of the mass of Earth's atmosphere is in the troposphere (the lowest layer of the atmosphere, from the ground to 8–14 km). The troposphere's components are relatively stable except for the amount of water (which is mainly as vapor). The variable water content causes fluctuations in refractive index that affect radio waves. The total vertical path delay due to water varies geographically, is up to 0.8 m and is independent of frequency [28, p. 524]. Weather and turbulence on a wide range of spatial and temporal scales cause fluctuations in the delay. The most demanding conditions for radar imaging are rapid changes over short-length scales, usually associated with severe weather. Some representative values of fluctuations that have typically caused problems for radar interferometry at mid-latitudes are given in Table II.

TABLE II
TROPOSPHERIC MOISTURE DATA FOR PHASE SCREEN MODELING. (VALUES CORRESPOND TO TYPICAL STRUCTURES CAUSING DIFFICULTIES FOR COMMERCIAL INSAR APPLICATIONS, BASED ON A CO-AUTHOR'S EXPERIENCE)

| Parameter | Value | Comments |
|---|---|---|
| Windspeed | 10 m $s^{-1}$ | Typical value |
| Wavelength | 10–30 km | Assume 20 km |
| Amplitude | 5–20 mm | Assume 10 mm (1-way, vertical, mean-to-peak) |
| Height | 2 km | Mean for moisture |

### B. Orbit

For our purposes, GEO orbits have the same period as Earth's rotation (rather than some other multiple of the period). This means that the semi-major axis $a$ is 42 164 km. Other orbit parameters that can be chosen are inclination $i$, eccentricity $e$, right ascension of the ascending node (RAAN) $\Omega$, and argument of perigee $\omega$.

The GEO region is regulated by the International Telecommunications Union (ITU) because of its commercial value [29]. Communication satellites are allocated specific bands in the radio spectrum together with an orbit location specified by its longitude around the equatorial ring. The satellite is required to station-keep within a tolerance of $\pm 0.1^\circ$ ($\pm 73.6$ km) in longitude. Limits on eccentricity and inclination are not currently specified but both are usually close to zero for operational communication satellites so that displacements from the nominal position are only a few times 10 km at most. Regular station-keeping maneuvers are necessary to counteract perturbations: these are typically done a few times a month.

Some GEO SAR concepts assume orbits, which significantly exceed the standard ITU allocation. It is often possible to make appropriate changes to eccentricity so that the satellite does not cross too close to the GEO ring (within about 200 km of the geostationary height at the equator).

For SAR motion is needed to synthesize the aperture. Synthetic apertures compatible with the current ITU guidelines can therefore have a maximum size of around 100 km. The orbit inclination and eccentricity and their relative phasing (i.e., $e$, $i$, $\Omega$, $\omega$) can be chosen to create various shapes and sizes of relative orbit. A convenient model for these small displacement orbits about a nominal geostationary point is defined by the Hill's equations [30, p. 393].

Expressions for orbit speed relative to Earth for circular GEO orbits with inclination $i$ at equator crossing and the north or south extremes can be written in terms of the inertial orbit velocity $v_G = 3075$ m $\cdot$ $s^{-1}$. Thus

$$v = 2v_G \sin i/2 \qquad \text{(equator crossing)} \tag{2}$$

$$v = v_G(1 - \cos i) \qquad \text{(N and S extremes)}. \tag{3}$$

An orbit only slightly displaced from geostationary with a relative orbit diameter of $d$ has a maximum azimuthal speed of $v = \pi d/T_{\text{day}}$ ($T_{\text{day}}$ is one sidereal day).

*1) Manoeuvres:* A further practical constraint on satellite orbits is that "large" maneuvers are expensive: satellites do not significantly change orbit once their initial orbit is established. The cost is quantified in terms of the velocity change $\Delta V$ required for the maneuver since this directly relates to the change in orbit and can be converted to required propellant mass simply. In the GEO region, maneuvers equivalent to about 50 m $\cdot$ $s^{-1}$ are needed each year to counteract perturbations [31, p. 138] (which are primarily due to the gravity fields of the Sun and Moon); over a typical comsat lifetime of 15 years this amounts to 750 m $\cdot$ $s^{-1}$, which is a significant cost to the mission. Modern satellites increasingly use low-thrust electric propulsion for station-keeping because of its mass efficiency.

High-inclination orbits will be also subject to orbit perturbations and will require an appropriate propulsion system and fuel load. However, some moderate inclination orbits ($i \simeq 7.5^\circ$) are quasi-stable [32, p. 219] and require much less orbit maintenance. These orbits offer interesting possibilities for long lifetime GEO SAR missions.

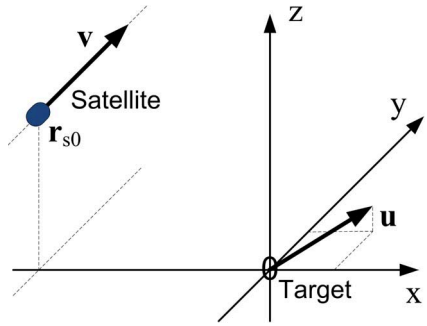


Fig. 1. Satellite and target geometry for calculating apparent azimuth shift due to target motion. At $t = 0$, the target is at the origin and the satellite at $\mathbf{r}_{s0}$.

### C. SAR Image Focusing

SAR image focusing is the process of forming the radar image from the raw signal time series that contains responses for targets at all azimuth positions within a given range gate. Signals for a particular azimuth position have a unique phase history: the image focusing process allocates the response for targets with this specific phase history to the (complex) backscatter value for that particular azimuth position. Standard SAR focusing algorithms assume that targets are static and that the atmosphere above them does not change.

However, coherent changes in signal phase during signal integration (e.g., due to target motion in the slant range direction) result in image artifacts. A LEO SAR example is the along-track displacement of moving targets, such as ships. For GEO SAR, the effects are more pronounced because of the increased range. Motion of individual scatterer results in azimuth shifts as for LEO SAR, but in addition, phase changes common to a group of pixels can cause an appreciable azimuth shift of that part of the image in GEO SAR (perhaps due to atmospheric changes).

*1) Target Motion, Clutter:* Fig. 1 shows the geometry used to derive the azimuth shift due to target motion (based on Rees [33, p. 305]). The satellite crosses the $Oxz$ plane at $t = 0$ moving parallel to the $y$-axis. At $t = 0$, the target is at the origin with velocity $\mathbf{u}$. For the broadside geometry assumed, a static target's $y$ position is the satellite position when the Doppler shift is zero; this condition also gives the apparent position of a moving target. The zero Doppler condition is $\mathbf{r}' \cdot \mathbf{v}' = 0$, where

TABLE III
APPROXIMATE SCALES OF CONTRIBUTIONS TO CHANGE IN SLANT PATH PHASE DUE TO SATELLITE MOTION AND PHASE RATE, COMPARING LEO AND GEO SAR SYSTEMS. PERTURBATION PARAMETERS ARE FROM TABLES I AND II; LEO AND GEO ORBIT HEIGHTS AND VELOCITIES ARE 800 km, 23 440 km (FOR A LATITUDE OF 45°), AND 7.45 km · s$^{-1}$ AND 2.5 m · s$^{-1}$, RESPECTIVELY

| Layer | Height | Perturbation | | | | LEO | | GEO | |
|---|---|---|---|---|---|---|---|---|---|
| | | Speed | Size | $\omega$ | $k$ | $v_i$ | $\mathbf{v}_i.\nabla\phi$ | $v_i$ | $\mathbf{v}_i.\nabla\phi$ |
| | km | m s$^{-1}$ | km | mrad s$^{-1}$ | mrad m$^{-1}$ | m s$^{-1}$ | mrad s$^{-1}$ | m s$^{-1}$ | $\mu$rad s$^{-1}$ |
| Ionosphere | 300 | 250 | 300 | 5.24 | 0.021 | 2794 | 58.5 | 0.0320 | 0.67 |
| Troposphere | 1.5 | 10 | 20 | 3.14 | 0.314 | 14 | 4.4 | 0.0002 | 0.05 |

$\mathbf{r}'$ and $\mathbf{v}'$ are the relative position and velocity of satellite and target. Thus

$$\mathbf{r}' = (\mathbf{r}_{s0} + \mathbf{v}t) - \mathbf{u}t, \quad \mathbf{v}' = \mathbf{v} - \mathbf{u}$$
$$\mathbf{r}' \cdot \mathbf{v}' = (\mathbf{r}_{s0} + (\mathbf{v} - \mathbf{u})t) \cdot (\mathbf{v} - \mathbf{u}). \tag{4}$$

Hence, the apparent target azimuth offset $\delta y$ to first order (noting $\mathbf{r}_{s0} \cdot \mathbf{v} = 0$) is its position at time $t_0$ given by

$$0 = (\mathbf{r}_{s0} + (\mathbf{v} - \mathbf{u})t_0) \cdot (\mathbf{v} - \mathbf{u})$$
$$t_0 = -\frac{\mathbf{r}_{s0} \cdot (\mathbf{v} - \mathbf{u})}{(\mathbf{v} - \mathbf{u}) \cdot (\mathbf{v} - \mathbf{u})} = \frac{\mathbf{r}_{s0} \cdot \mathbf{u}}{|\mathbf{v} - \mathbf{u}|^2}$$
$$\delta y = vt_0 = v\frac{\mathbf{r}_{s0} \cdot \mathbf{u}}{|\mathbf{v} - \mathbf{u}|^2}. \tag{5}$$

Equation (5) gives much larger azimuth offsets for GEO SAR than for LEO SAR because the slant range is larger and the relative velocity may be far smaller. Moving targets and clutter can therefore have large apparent azimuth displacements. The following are the two qualifications that apply.

1) The motion should be coherent for the full integration time, which may be several minutes or longer.
2) Pulse compression and azimuth presumming can filter out returns above a critical speed $v_c$, which may be very low [11].

The minimum pulse-repetition frequency (PRF) is set to avoid azimuth ambiguities. If the actual PRF is greater than this, then presumming can be used to filter out high Doppler frequencies due to clutter and thus reduce the image degradation due to clutter. This is discussed in more detail by [11], [34].

Slow steady motion during image formation can still give appreciable azimuth shifts (e.g., 0.1 mm · s$^{-1}$ can lead to shifts of several × 100 m). Such motion might be due to thermal expansion of buildings or other structures.

*2) Temporal Change in Refractive Index:* Changes of the refractive index along the slant path from the radar to the target can cause image artifacts or defocusing. The change may be due to temporal or spatial variation of refractive index: for GEO SAR, the temporal changes become important. The rate of change of phase at the intersection between the slant path from radar to target and the phase screen is due to the temporal change of the phase screen at that point $(\partial\phi/\partial t)$ plus the scalar product between the APS spatial gradient and the intersection point velocity. This ensures, for example, that if the intersection point moves at the advection velocity of a "frozen" phase screen then no phase change occurs. If $\mathbf{v_i}$ is the velocity of the intersection point, the total rate of change $d\phi/dt$ is

$$\frac{d\phi}{dt} = \frac{\partial\phi}{\partial t} + \mathbf{v_i} \cdot \nabla\phi. \tag{6}$$

Assuming a simple sinusoidal phase disturbance (7), the fractional rate of change of phase is given by (8). Typical values of these terms for LEO and GEO are shown in Table III. In LEO, the high satellite velocity means that spatial variation $(\mathbf{v_i} \cdot \nabla\phi)$ of refractive index is important. However, in GEO satellites tend to have lower speeds and then the temporal variation $(\partial\phi/\partial t)$ dominates. Thus

$$\phi = \phi_1 e^{i(\mathbf{k}\cdot\mathbf{r} - \omega t)} \tag{7}$$

$$\frac{1}{\phi}\frac{d\phi}{dt} = -i\omega + i\mathbf{v_i} \cdot \mathbf{k}. \tag{8}$$

The phase rate causes an azimuth shift. Appendix A shows that this shift $\delta y$ depends on wavelength, azimuthal velocity, slant range and rate of phase change. Using (20), the shift can be expressed in terms of the azimuth resolution $\Delta y$ (10)

$$\delta y = \frac{r\dot{\phi}\lambda}{2\pi v \cos\theta(\mathbf{e}_2 \cdot \mathbf{e}_a)} \tag{9}$$

$$= \frac{\Delta y t_{\text{int}}\dot{\phi}}{\pi \cos\theta}. \tag{10}$$

Azimuth shifts in SAR images due to atmospheric perturbations have been previously reported by several authors over the last 50 years (e.g., [19], [21]–[23], [35]). However, the shift has not been explicitly related to the phase rate, nor used to measure phase rate from azimuth displacement. A suitable image sequence from GEO SAR provides an opportunity to make this measurement of $\dot{\phi}$. It should be possible to track both strong point targets (giving $\dot{\phi}$ at pixel scale) and image features (giving $\dot{\phi}$ at the scale of a group of pixels), depending on the image properties and the scale of atmospheric perturbations. Since in some circumstances, the azimuth shift is several times the azimuth resolution, it should be easily measurable.

This azimuth shift may be significant for GEO SAR since it allows the phase screen to be estimated without needing persistent scatterers. To estimate typical magnitudes, the phase rate can be taken to be due to a change of $\delta z = 10$ mm of one-way zenith optical path length due to tropospheric humidity over $l = 20$ km horizontally, this pattern being advected over the target at $w = 10$ m · s$^{-1}$. This gives a phase rate at C-band $(\lambda = 5$ cm) of $\dot{\phi} = 2\pi w\delta z/(l\lambda) = 6 \times 10^{-4}$ rad · s$^{-1}$ approximately. Table IV shows the estimated azimuth shifts due to this phase rate in LEO and in GEO. The shift in LEO is negligible but for GEO SAR, it becomes appreciable (and therefore allows the APS rate of change to be measured in principle). Results from a GEO SAR simulator are consistent with this model of the azimuth shift due to the APS temporal change [8].

TABLE IV
EXAMPLE VALUES OF AZIMUTH SHIFT EXPECTED FOR LEO AND GEOSYNCHRONOUS GEO ORBIT SAR IMAGING DUE TO TEMPORAL CHANGE IN APS OF $6 \times 10^{-4}$ rad $\cdot$ s$^{-1}$ (ONE-WAY, ZENITH)

| Parameter | LEO | GEO |
|---|---|---|
| Slant range (km) | 850 | 40000 |
| Velocity (m s$^{-1}$) | 7500 | 2 |
| Incidence ($^\circ$) | 23 | 50 |
| Azimuth shift (m) | 0.0006 | 156 |

### D. Spatial and Temporal Averaging

SAR imaging inherently averages in space and time. Spatial averaging is within the point target response, and temporal averaging is during the integration period. Quantifying the effects of temporal averaging is important to understand, which temporal changes, particularly clutter and the APS, may affect image focusing.

The APS at any point changes with time. Linear phase changes within the integration time cause azimuth shifts but do not otherwise (to first order) corrupt the image. However, deviations from linearity cause loss of focus. The effects of the nonlinear phase change on image quality need to be quantified to ensure that the system design does not exceed acceptable limits.

We model temporal phase screen changes using sinusoidal components. The sinusoid is analyzed as a linear best fit $(\hat{m}t + \hat{c})$ plus nonlinear deviations $\delta\phi(t)$ from this (11). It is assumed that the focusing algorithm will displace the target according to the linear component and that the nonlinear deviation from the linear change causes loss of focus. The loss of focus is quantified by the amplitude reduction of the phasor integral ($y()$, (12)). Thus

$$\Delta\phi(t) = a\sin(\omega t + \psi_0) = (\hat{m}t + \hat{c}) + \delta\phi(t) \tag{11}$$

$$y(\psi_0, t_1, \omega\Delta t, a) = \frac{1}{\Delta t}\int_{t_1-\Delta t/2}^{t_1+\Delta t/2} \exp\left(i\delta\phi(t)\right) dt. \tag{12}$$

In the limit of small sinusoid amplitudes $a$ and time intervals $\Delta t$ (expressed as phase interval $\omega\Delta t$) $y$ is 1. As $a$ and $\omega\Delta t$ increase, $y$ decreases. There is modest dependence on the initial phase offsets $\psi_0$ and $t_1$, thus $y()$ has been numerically evaluated for all initial phases to give gain $\overline{y}(\omega\Delta t, a)$: the lowest gain values over all phase offsets are plotted in Fig. 2, where $a$ is the screen amplitude, and $\omega\Delta t$ is the phase interval.

For system design, it is useful to quantify the limits within which temporal averaging can be ignored. We choose the contour $\overline{y} = 0.95$ (contours for $\overline{y} = 0.9$ or 0.8, for example, might also have been chosen; note that this is the gain for amplitude, not intensity). This can be approximated (see Appendix B) by the fitting functions

$$a = a_{95}(a_{95} = 0.45 \text{ rad}) \qquad \text{for } \omega\Delta t \geq \psi_{0:95} \tag{13}$$

$$\omega\Delta t = \frac{c_{95}}{\sqrt{a}}\left(c_{95} = 2.9 \text{ rad}^{\frac{3}{2}}\right) \qquad \text{for } a \geq a_{95}$$

$$\psi_{0:95} = \frac{c_{95}}{\sqrt{a_{95}}} \simeq 4.32 \text{ rad}. \tag{14}$$

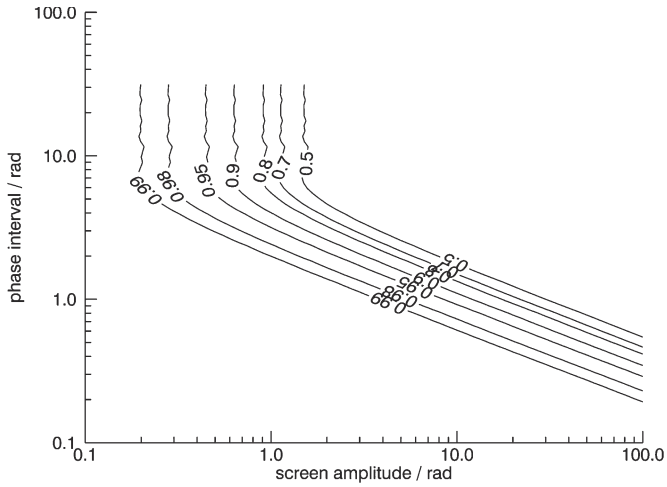


Fig. 2. Signal attenuation due to nonlinearity of APS time variation: contours are of worst integration gain over all phase offsets [$a$ is the screen amplitude and $\omega\Delta t$ is the phase interval of (12)].

If $a$ or $\omega\Delta t$ are smaller than these values, then the gain is greater than 0.95, and temporal averaging does not cause significant degradation.

The phase amplitude for two-way propagation at incidence angle $\theta$ is estimated using (15) and (16) where $\delta_i$, $\delta_t$ is the vertical delay amplitude (mean to peak) due to the ionosphere or troposphere, respectively. The ionospheric delay increases with wavelength, whereas the tropospheric phase delay decreases

$$\phi_i = \frac{4\pi}{\lambda\cos\theta}\,\delta_i = \frac{4\pi K\text{TEC}\lambda}{c^2\cos\theta} \tag{15}$$

$$\phi_t = \frac{4\pi}{\lambda\cos\theta}\,\delta_t. \tag{16}$$

Equations (14)–(16) and (20) are used to give the change in azimuth resolution $\Delta y$ with integration time $t_{\text{int}}$ along the contour of averaging gain (for $a \geq a_{95}$). Equations (17) and (18) give these expressions for ionospheric and tropospheric perturbations, respectively (by substituting the wavelength parameter). Thus

$$t_{\text{int}}^{\frac{3}{2}} = \frac{c_{95}c}{\omega}\sqrt{\frac{r\cos\theta}{8\pi K\text{TEC}v\Delta y}} \tag{17}$$

$$t_{\text{int}} = \left(\frac{c_{95}}{\omega}\right)^2 \frac{\Delta y v\cos\theta}{2\pi r\delta_t}. \tag{18}$$

### E. Radar Design Constraints

Radar system design is complex because so many parameters are interrelated. For initial system design, however, three main constraints should be accounted for.

*1) Spatial Resolution:* Spatial resolution is a primary user requirement. The natural radar coordinates are range and azimuth.

Range resolution is determined by the bandwidth $\Delta f$ of the transmitted pulse. For a conventional monostatic configuration (transmitter and receiver in the same place) slant range resolution $\Delta r$ is equal to half the pulse length $c\tau/2 = c/(2\Delta f)$ because the radiation travels out and back. $\Delta r$ projected on

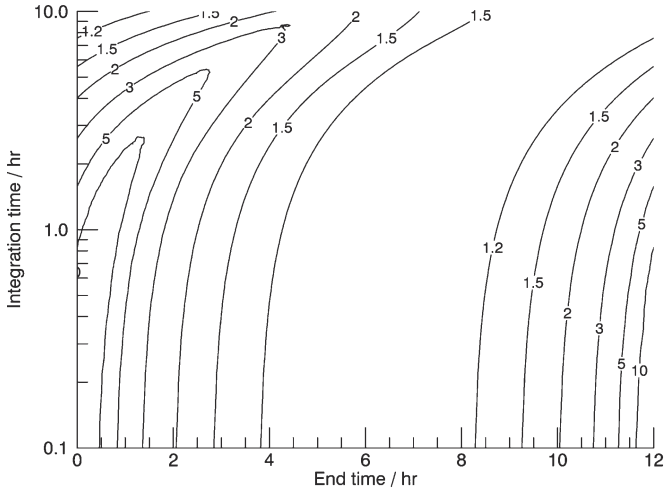


Fig. 3. Contours of azimuth resolution degradation factor $f$ as a function of integration time $t_{\rm int}$ and end time of the image $t_{\rm end}$ during the orbit assuming sinusoidal motion (the satellite is at the limits of the azimuthal motion at 0 and 12 h). For a given integration time $\Delta y(t_{\rm int}, t_{\rm end}) = f\Delta y_0(t_{\rm int})$, where $\Delta y_0(t_{\rm int})$ is the best resolution that can be achieved for that integration time.

Earth's surface (incidence angle $\theta$) gives the across-track resolution $\Delta x$

$$\Delta x = \frac{\Delta r}{\sin\theta} = \frac{c\tau}{2\sin\theta} = \frac{c}{2\Delta f \sin\theta}. \tag{19}$$

Azimuth resolution is determined by the aperture size parallel to Earth's surface and perpendicular to the range direction. For SAR, the effective aperture is synthesized by moving a real aperture during the signal integration time; full resolution is achieved through numerical processing of the received signals. The angular resolution for an aperture of length $d$ at wavelength $\lambda$ is $\delta\alpha = \lambda/d$ if the radiation passes once through the aperture. For a monostatic radar, the radiation passes out and back through the same aperture, and the angular resolution improves to $\delta\alpha = \lambda/2d$ (many texts ignore or fudge the extra factor $1/2$; [23] includes it correctly). For GEO SAR imaging, spotlight mode may be used and the synthesized antenna length is the integral of satellite velocity relative to Earth in the azimuth direction $\int vdt$ (or velocity multiplied by integration time $t_{\rm int}$ for short periods; this may be less than the full beamwidth). The azimuth resolution is $r$ multiplied by angular resolution [ignoring orbit curvature, (20)]

$$\Delta y = r\delta\alpha = \frac{r\lambda}{2vt_{\rm int}}. \tag{20}$$

Choosing spatial resolution thus implies constraints on transmitted bandwidth, slant range, wavelength, integration time, and satellite velocity. It is important to note that (azimuthal) satellite velocity changes during the orbit. It typically sinusoidally varies and thus falls to zero at the extremes of the motion. This degrades azimuthal resolution from that possibility when speed is higher, and for motion over a significant portion of the 24-h period, the sinusoidal variation should be accounted for. Fig. 3 assumes sinusoidal azimuthal motion and shows how the azimuthal resolution degrades relative to the best value achievable for a given integration time as a function of the end time of the image acquisition. For example, $t_{\rm int} = 0.2$ h ending at 4 h has resolution 20% worse than if it were to end near 6 h, whereas if $t_{\rm int} = 3$ h ending at 2 h, azimuth resolution is about five times worse. Best resolution is achieved when the integration time is centered on 6 h, since speed is highest then. Integration periods, which include times of very low speed, are of little use since resolution is badly degraded. This daily variation (1 sidereal day) has significant operational implications. The variation in azimuthal velocity also affects signal-to-noise ratio (SNR) $S$ and imaging ambiguities: in general, a lower speed allows more time for signal integration and thus improves $S$ and reduces azimuth ambiguities.

*2) SNR:* A fundamental radar requirement concerns image quality. This is conventionally described by the SNR $= S$ achieved for a given spatial resolution. Equation (21) shows how $S$ depends on other system parameters (effective mean transmitted RF power $P_t f_t$, spatial resolution $l$ assumed equal in range and azimuth, surface backscatter $\sigma^0$ and incidence angle $\theta$, antenna area $A$, receiver noise factor $F_n$ and surface temperature $T_s$; $k$ is Boltzmann's constant). The equation can be derived from equation 11 of [5] (apart from the factor $\cos\theta$, accounting for the local incidence angle) and assumes coherent integration of signals during $t_{\rm int}$. Pulse compression is parameterized by the duty cycle factor $f_t$. The equation ignores RF signal losses and therefore should be interpreted to give the *effective* transmitter power $P_{t,\rm eff}$, where the *actual* RF power needed $P_{t,\rm act} = P_{t,\rm eff}/\eta$ and $\eta$ is the RF efficiency factor

$$S = \frac{P_t f_t t_{\rm int} l^2 \sigma^0 A^2 \cos\theta}{4\pi\lambda^2 r^4 F_n k T_s}. \tag{21}$$

Equations (21) and (23)–(25) should be interpreted with caution. They assume that range and azimuth resolution are equal: in practice, this may not be the case. An appropriate choice of $S$ and $l$ requires careful evaluation of the system requirements and of the APS compensation method. For high-resolution backscatter images, the optimal design will emphasize spatial resolution and accept a low $S$ since the backscatter image quality can be improved with multilooking. If the user requires high-quality phase information (e.g., for interferometry) then high $S$ is needed that tends to compromise spatial resolution.

APS compensation brings additional requirements and is an area of active research. Several APS estimation methods have been suggested: good spatial resolution and signal quality help all of them, but optimal solutions have not yet been clearly identified. Good relevant work in this area is provided by [9], [10], [12], [13], [36]. Since APS compensation may start with coarse resolution, short $t_{\rm int}$ images during which the atmosphere is assumed quasi-static, the azimuth resolution may be severely degraded relative to the final image. However, the product of integration time and azimuth resolution is determined by velocity and does not change significantly between the coarse and fine images: $S$ therefore does not degrade for the coarse resolution images, and in fact can be improved by averaging pixels in the range direction to equalize range and azimuth resolution in the coarse images.

*3) Image Ambiguities—Antenna Size:* Range and azimuth ambiguities occur if the radar pulses transmitted are too frequent or too sparse. To derive the limits, we assume a

rectangular aperture $d_1 \times d_2$, with $d_1$ the dimension across-track and $d_2$ along-track. To avoid range ambiguities (only one pulse's return from the illuminated area received at any moment) the maximum pulse-repetition frequency $n_{\mathrm{PRF}}$ is $cd_1/(4R\lambda \tan\theta)$. To avoid azimuth ambiguities (ambiguous directions must lie outside the illuminated footprint) requires a minimum $n_{\mathrm{PRF}}$ of $2v/d_2$. The requirement that the minimum value must be less than the maximum defines a minimum for the product $d_1 d_2$, i.e., a minimum antenna area $A_{\min}$. This antenna size ensures that imaging ambiguities fall outside the antenna footprint and therefore can be ignored. In some cases, this requirement is excessive, e.g., if the beam footprint exceeds the Earth disk, and then, a smaller antenna can be used. Thus

$$\frac{2v}{d_2} < n_{\mathrm{PRF}} < \frac{cd_1}{4r\lambda \tan\theta}, \quad A_{\min} = \frac{8vr\lambda \tan\theta}{c}. \tag{22}$$

If an area larger than $A_{\min}$ is used, then there is some freedom to choose $n_{\mathrm{PRF}}$, and azimuth presumming can be used to reduce the data rate.

The antenna size depends on (azimuthal) velocity $v$. Since this varies during an orbit, the required antenna size is a function of orbit position in principle: system design must generally accept the worst case sizing. High-inclination orbits can result in speeds over 1 km $\cdot$ s$^{-1}$, which require very large antennas; this can be ameliorated using squint imaging to reduce the azimuthal velocity component.

Many other factors also affect SAR system design, but those listed here quantify the primary requirements.

## III. System Design Process

The aim of system design is to identify a set of parameters, which define a feasible GEO SAR system meeting given requirements. For GEO orbits, the key parameters, which the designer can choose, are $v$ (the azimuthal velocity component, i.e., the choice of orbit), wavelength $\lambda$, spatial resolution $l$, and integration time $t_{\mathrm{int}}$ [these are themselves interrelated, (20)]. The principal requirement is usually spatial resolution, although wavelength and integration time may be also important.

Equation (20) relates integration time $t_{\mathrm{int}}$, spatial resolution $l$, wavelength $\lambda$ and (azimuthal) orbit speed $v$. Equation (21) can be therefore rewritten to give antenna area $A$ in terms of any three of these parameters (23)–(25). As above, the equations assume equal resolution in range and azimuth and are in terms of *effective* rather than *actual* transmitted RF power. Thus

$$A^2 = \frac{4\pi r^4 S F_n k T_s}{P_t f_t \sigma^0 \cos\theta} \cdot \frac{\lambda^2}{t_{\mathrm{int}} l^2} \tag{23}$$

$$= \frac{16\pi r^2 S F_n k T_s}{P_t f_t \sigma^0 \cos\theta} \cdot v^2 t_{\mathrm{int}} \tag{24}$$

$$= \frac{8\pi r S F_n k T_s}{P_t f_t \sigma^0 \cos\theta} \cdot \frac{\lambda v}{l}. \tag{25}$$

Equations (23)–(25) show how antenna size scales with system parameters, such as $v$, $P_t f_t$, $\lambda$, resolution $l$, and integration time. In particular, the required diameter is proportional to $(P_t f_t)^{-1/4}$, to $(l/\lambda)^{-1/4}$ and to $v^{1/4}$ (these parameters then determine $t_{\mathrm{int}}$). Thus, increasing mean transmitted power by a factor of 10 reduces the required antenna diameter to 56% of its original size.

A two-step process for initial system design is presented here. The first step considers the tradeoff between wavelength, integration time, and spatial resolution for a given orbit (Fig. 4). This step addresses the orbit, atmospheric perturbation, and averaging constraints. The second step then calculates the antenna size needed for a given mean transmitter power and integration time, which ensures the SNR and antenna area constraints are satisfied.

The first step is illustrated in Fig. 4. The significant atmospheric length and timescales are plotted in Fig. 4(a). The dark shading shows the scales defined in Tables I and II. Choosing an orbit defines the (maximum) azimuthal velocity component: for a 50-km diameter relative orbit, this is 1.8 m $\cdot$ s$^{-1}$ (as used for Figs. 4 and 5). Once the speed is defined, the spatial resolution as a function of integration time for a given wavelength is known (20). Fig. 4(b) adds this information. For initial design, the figure can be redrawn for various values of velocity to represent different points on the orbit—a more sophisticated dynamic model should be used for later design stages.

Once the orbit is chosen (defining azimuthal speed), the length and timescales that effectively plot has coordinates of $t_{\mathrm{int}}$ and wavelength $\lambda$. The wavelength determines the perturbation phase amplitude [e.g., 5-mm zenith path variation in the troposphere corresponds to 1.26 rad for a two-way vertical path with $\lambda = 5$ cm, (16)]. The averaging constraint functions that approximate the gain contour (14) can be therefore mapped onto the length and timescale plot, see Fig. 4(c). Table V shows the perturbation cases used and the wavelengths beyond which the perturbations can be ignored (longer wavelengths for tropospheric perturbations, shorter ones for the ionosphere). Shading indicates regions where averaging gain is 0.95 or less (blue for ionospheric perturbations, green for the troposphere). Two depths of shading are used for each: the ionospheric conditions represent medium and large-scale TIDs. Large-scale TIDs are rare but restrict integration times significantly. Medium-scale TIDs are more frequent and less restrictive. Two scales of tropospheric disturbance are represented: the most difficult imaging conditions are due to short wavelength structures. In Fig. 4(c), system designs that do not need atmospheric phase compensation for focusing are in the unshaded region.

Fig. 5 shows the SNR and antenna area constraints. Equation (21) is rewritten to give antenna area, and thus, diameter of a circular antenna, as a function of transmitted power, integration time and azimuthal speed [(24), nonvarying parameter values are given in Table VI]. A high value of SNR is assumed (20 dB) since accurate backscatter phase measurements are wanted for the APS retrievals (20 dB in power corresponds to SNR $= 10$ for the electric field phasors, i.e., a phase error $\simeq$0.1 rad). If the system were designed primarily to create backscatter images then a better design solution would be to reduce the SNR, perhaps as low as a few dB, and to use the extra capability to achieve finer spatial resolution. Multilooking then provides images with good spatial resolution and reduced noise (the uncertainties due to speckle and measurement noise are more balanced using this approach).

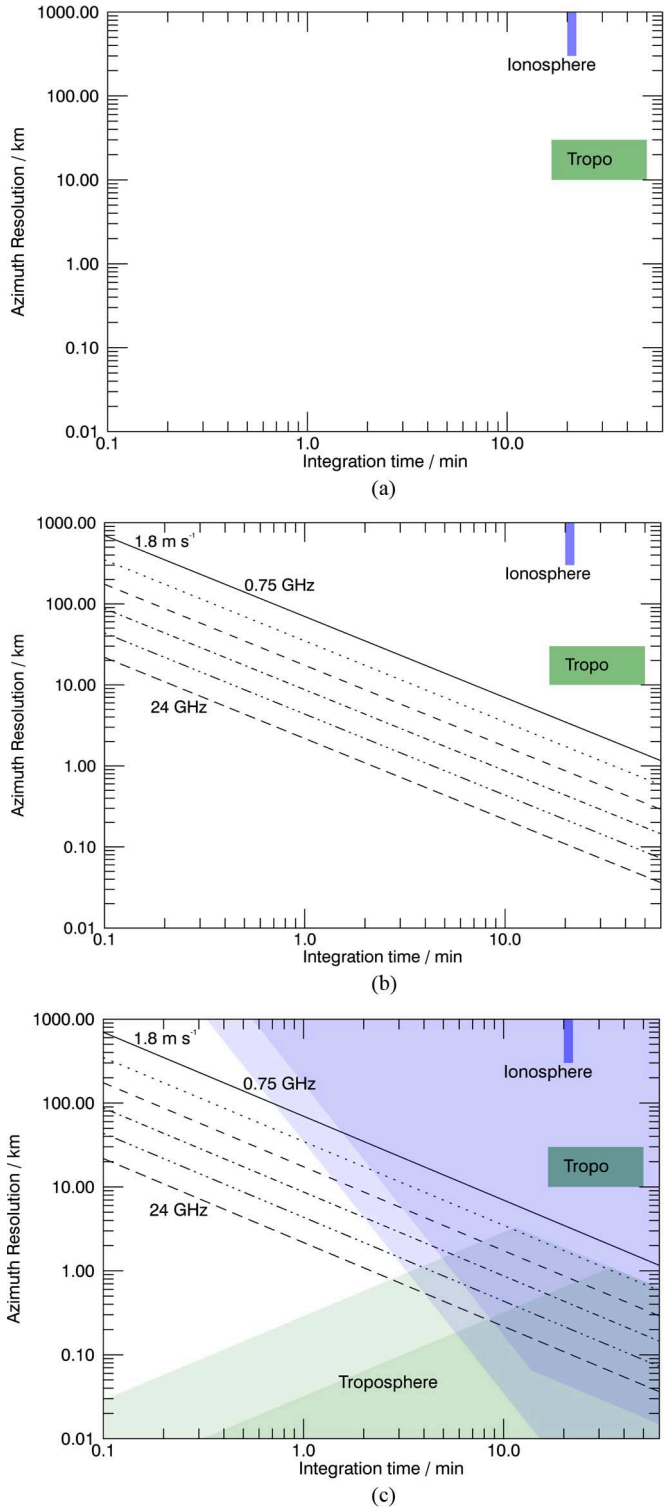


Fig. 4. Development of the length and timescale plot summarizing system design options for a given orbit (relative diameter 50 km, $v_{\max} = 1.8\,\mathrm{m} \cdot \mathrm{s}^{-1}$). (a) Atmospheric perturbation length and timescales. (b) Atmospheric perturbations and azimuth resolution for the chosen orbit and frequencies of 0.75, 1.5, 3, 6, 12, and 24 GHz. (c) Atmospheric perturbations, azimuth resolution, and averaging constraints (images formed using $t_{\mathrm{int}}$ from unshaded regions do not need atmospheric phase correction).

Antenna diameter is plotted in Fig. 5(a) [the same function applies for all wavelengths, (24)]. Fig. 5(b) adds lines showing the minimum antenna size [which depends on speed and wavelength, (22)] for frequencies between 0.75 and 24 GHz (as in

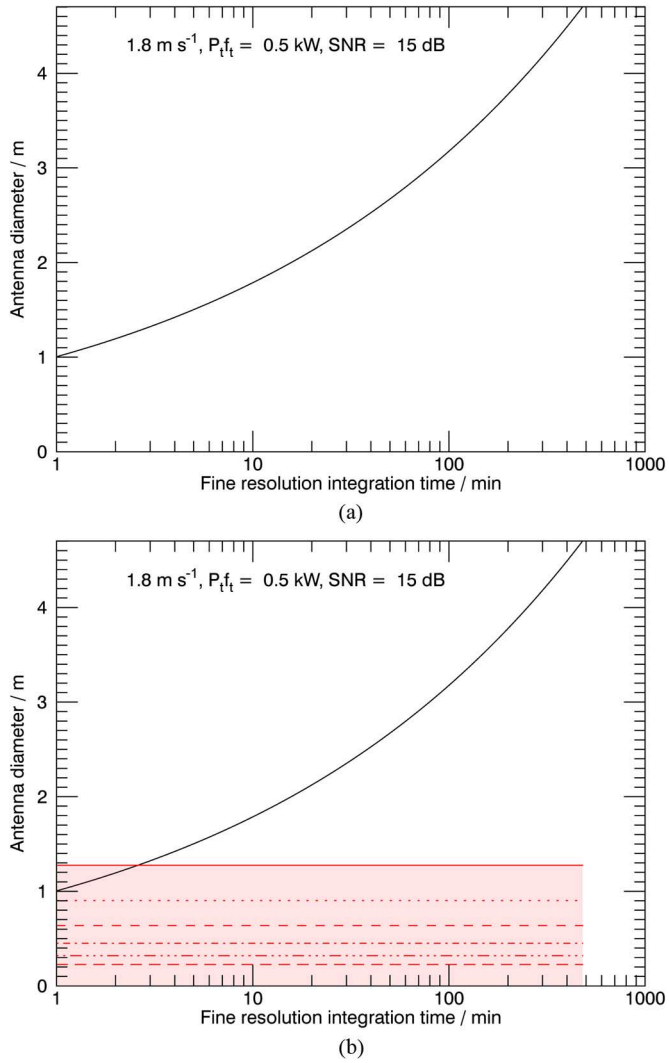


Fig. 5. Antenna diameter as a function of integration time for an effective mean transmitted power of 500 W, $S = 15$ dB and constant orbit speed of $1.8\,\mathrm{m} \cdot \mathrm{s}^{-1}$. (a) Antenna diameter as a function of integration time. (b) Antenna diameter as a function of integration time with shading showing limits of minimum antenna size for $n = 0.75, 1.5, 3, 6, 12,$ and 24 GHz (shaded, and using the same line styles as Fig. 4).

TABLE V
ATMOSPHERIC PERTURBATION CASES USED TO CALCULATE THE AVERAGING LIMIT CONTOURS AND THE CORRESPONDING WAVELENGTH LIMITS (AMPLITUDE IS ONE-WAY ZENITH PATH, A TWO-WAY PATH WITH INCIDENCE 45° IS USED TO CALCULATE WAVELENGTH; THE IONOSPHERE CASES REPRESENT LOW AND HIGH SOLAR ACTIVITY)

| Case | Perturbation amplitude (horizontal size) | Angular frequency mrad $\mathrm{s}^{-1}$ | Wavelength limit |
|---|---|---|---|
| Troposphere | 5 mm (10 km) | 6.28 | 0.197 m |
| Troposphere | 5 mm (30 km) | 2.09 | 0.197 m |
| Ionosphere | 1 TECU | 5.24 | 5.65 mm |
| Ionosphere | 6 TECU | 4.71 | 0.94 mm |

TABLE VI
PARAMETER VALUES FOR THE RESULTS OF FIGS. 5 AND 7

| Parameter | Value | Comment |
|---|---|---|
| $\sigma^0 \cos\theta$ | -20 dB | Surface backscatter |
| $T_s$ / K | 300 | Surface temperature |
| $r$ / km | 38000 | Slant range |
| $F_n$ | 5 | Noise figure (absolute) |

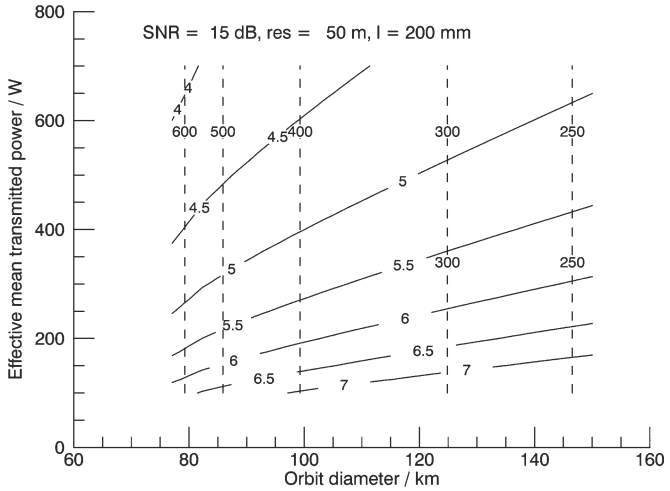


Fig. 6. Antenna diameter (meters, solid lines) and integration time (minutes, dashed lines) as a function of (low inclination) orbit diameter and effective transmitter power ($\lambda = 0.2$ m, 50-m resolution, 15-dB SNR; allowing for sinusoidal variation in azimuthal speed).

Fig. 4). Longer wavelengths need larger antennas: the shading indicates diameters smaller than that needed at 0.75 GHz, i.e., the most demanding case. It seems anomalous that a longer integration time requires a larger antenna; however, the increase in $t_{\rm int}$ implies improved spatial resolution, and it is this that drives the increase in size. An example alternative presentation of the antenna sizing is given in Fig. 6. This accounts for the sinusoidal orbit motion and shows the tradeoff between transmitter power and orbit (for low inclination orbits) for a given spatial resolution and frequency (which are often set by user requirements), and shows the antenna size and integration time required. In this case, orbit diameters below 77 km do not create a synthetic aperture large enough to give 50-m spatial resolution with $\lambda = 0.2$ m, and so, no solutions are shown. (It is assumed that the integration time is chosen optimally, cf. Fig. 3.)

These or similar diagrams can be used to identify feasible system designs. In particular, they identify systems that can achieve the desired azimuth resolution without needing atmospheric phase corrections to focus the image (i.e., in the unshaded region). Better resolution is possible, but only with phase compensation (the shading indicates which of the corrections—ionosphere and/or troposphere—are needed). Figs. 4 and 5 assume constant velocity. Over short periods, this is reasonable, but for $t_{\rm int}$ of several hours or near the extremes of the orbital motion it becomes important to account for the varying velocity.

Fig. 7 shows results for three orbits (100-km relative diameter, azimuthal speed 3.6 $\rm m \cdot s^{-1}$; 7.5° inclination, azimuthal speed $\sim$100 $\rm m \cdot s^{-1}$; 60° inclination, azimuthal speed $\sim$1500 $\rm m \cdot s^{-1}$; the effective azimuthal speed can be controlled to an extent using squint imaging). As the orbit speed increases, the azimuth resolution achieved for a given integration times improves. The perturbations depend on wavelength: long wavelengths are most affected by ionospheric perturbations, tropospheric humidity affects short wavelengths most. As the orbit speed increases, the required antenna sizes increase. For low speeds, the antenna is easily sized to avoid imaging ambiguities; however, as the speed increases this constraint becomes more demanding. It is important to note that the validity of the results depends on the accuracy of the input assumptions (e.g., the scales of the significant atmospheric perturbations).

This system design framework encompasses all the main GEO SAR concepts using near circular orbits; examples include:

- High-inclination orbits: azimuthal speed is high, thus fine resolution is possible, but this requires a large antenna and high power.
- Low inclination orbits: long integration times are needed to achieve fine resolution (and therefore, atmospheric phase corrections are needed); systems are feasible with modest power and antenna area.

Fig. 8 summarizes the key system design decision of whether or not atmospheric phase compensation will be needed to achieve the final desired spatial resolution. The threshold of 2–3 min is approximate (although consistent with other estimates, e.g., [9]); forming an image quickly enough to avoid the need for phase compensation tends to require large antennas and high power.

### A. Example System Designs

An example outline system design uses Fig. 7(a) and (b). To achieve 100-m spatial resolution at C-band ($f = 6$ GHz, dash–dot line) using a GEO SAR with relative orbit diameter 100 km, an integration time of about 45 min is needed [Fig. 7(a)]. This will require phase correction for both ionospheric and tropospheric perturbations. Every minute, the system can form an unperturbed image (with resolution of 4 km): the atmospheric phase corrections should be ideally derived from this time series. Fig. 7(b) shows that for $t_{\rm int} = 45$ min an antenna diameter of around 5.5 m will be required ($P_t f_t = 1$ kW), this is well above the minimum aperture diameter. Thus most of the key system parameters have been defined, and a design is achieved that satisfies all the main constraints.

The advantage of a graphical method of the outline system design as proposed here is that the designer can see easily whether design parameters are close to constraints or not. Further design iterations will use increasingly detailed quantitative methods.

### B. Atmospheric Phase Corrections

Atmospheric phase corrections or measurements are an important aspect of GEO SAR design and applications. Phase correction is needed if a sequence of coarse resolution images is used to estimate atmospheric phase so that the fine azimuth resolution image can be focused. In principle, the atmospheric phase is measurable in two ways.

- $\Delta\phi$: The phase due to the atmosphere (averaged over $t_{\rm int}$) adds to the backscatter phase: changes in this should therefore be directly measurable for suitable targets.
- $\dot{\phi}$: Linear rates of change of atmospheric phase will cause an azimuth shift, which itself is measurable.

Targets must remain stable, at least for the coarse resolution integration time, for $\Delta\phi$ and $\dot{\phi}$ to be measurable: unstable targets contribute to clutter. Since the atmospheric phase

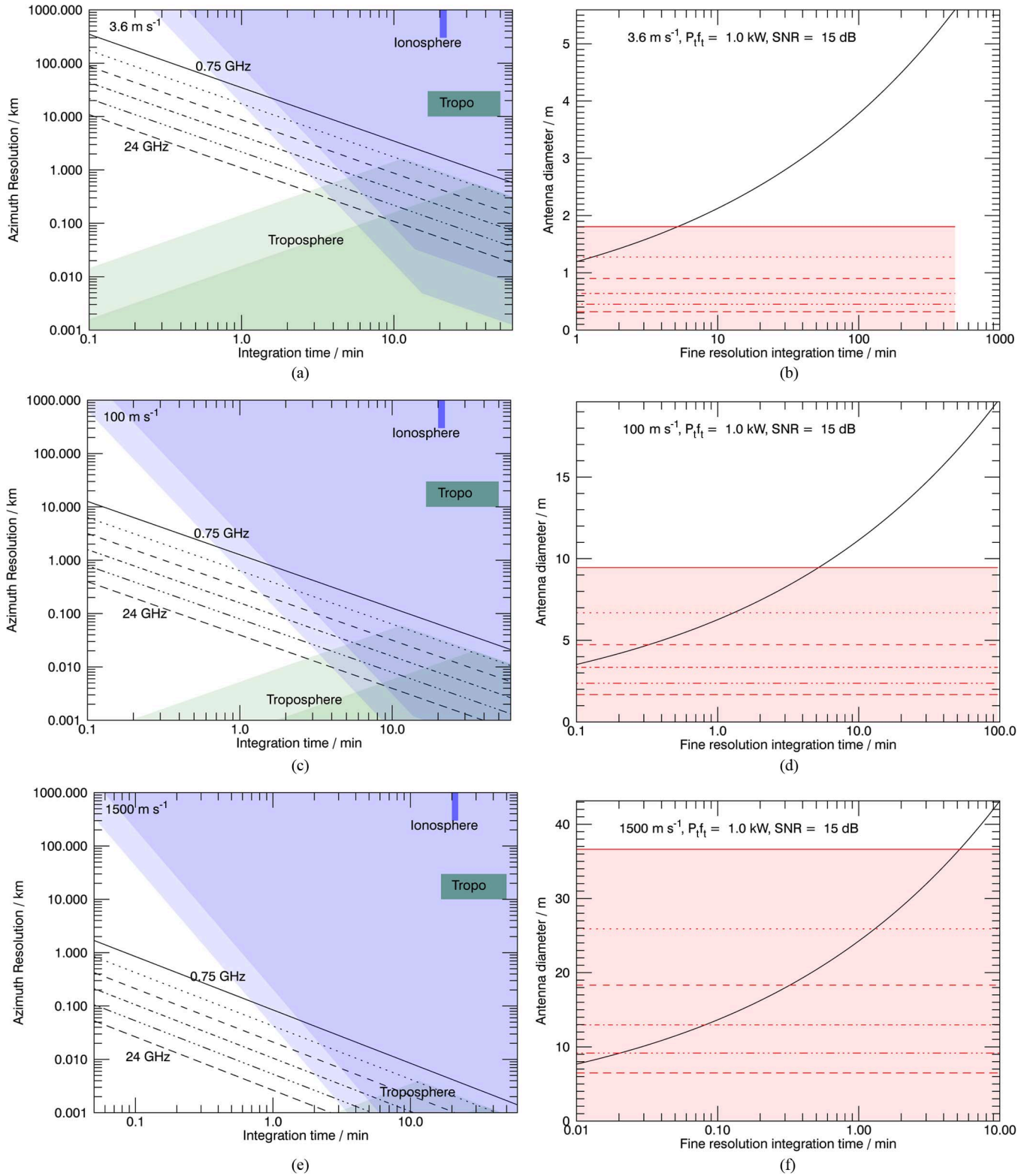


Fig. 7. System design charts for three candidate orbits illustrating the impact of atmospheric perturbations and the antenna sizing for a given mean effective power and SNR (using constant orbit speed approximation). (a) Resolution versus integration time (100-km orbit). (b) Antenna sizing (100-km orbit). (c) Resolution versus integration time (7.5° orbit). (d) Antenna sizing (7.5° orbit). (e) Resolution versus integration time (60° orbit). (f) Antenna sizing (60° orbit).

represents physical processes that can be modeled, data assimilation is an appropriate method for phase estimation. Two cases are likely to be encountered: i) targets that remain coherent throughout the integration time required to achieve fine azimuth resolution; or ii) incoherent targets.

The sequence of coarse resolution images of a natural surface, even a static one, will, in general, not be coherent with each other since they are formed using nonoverlapping segments of the satellite orbit. Areas that remain coherent are therefore likely to be ones dominated by a single persistent

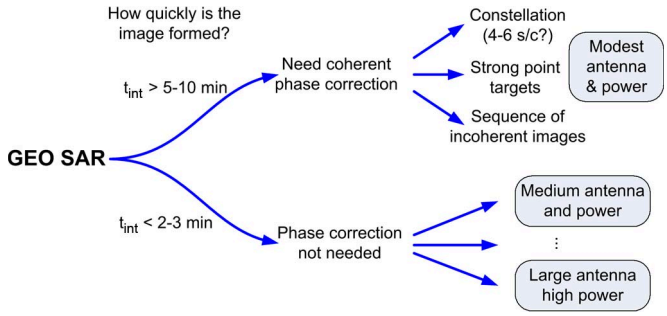


Fig. 8. GEO SAR imaging overview: whether atmospheric phase compensation is needed determines system design options.

scatterer (at the coarse resolution). The other way, in which the coarse images can be coherent with each other, is for the images to be taken using the same orbit segment: this requires a delay of 1 day or a constellation of satellites (perhaps with non-Keplerian orbits).

Unstable surfaces represent an important fraction of many scenes. These might be water surfaces or dense vegetation. At long wavelengths, even quite dense vegetation may be sufficiently stable (particularly in favorable weather conditions). Atmospheric structures strong enough to affect image focusing are typically kilometer or more in size, and thus, only a few stable areas every few km may be sufficient to estimate the APS adequately.

The following comments discuss the two target types and how the estimated APS can be used to form the fine resolution image.

*1) Coherent Targets:* If a dominant point target remains coherent through the fine resolution integration time, then phase and phase rate can be measured almost at pixel scale. If there is an azimuth offset between this target and the reference position assumed for SAR image focusing, then a phase due to this offset has to be corrected for.

*2) Incoherent Scenes:* For natural surfaces, the phase change will not be directly measurable since images in the sequence are not coherent. However, the phase rate will be sometimes measurable by tracking the azimuth shift of recognizable features in the image. The azimuth shift is most apparent for systems with low azimuthal velocity.

*3) Using the Atmospheric Phase Correction:* The atmospheric phase correction required is a function of (2-D) space and time—similar to the real atmosphere: $\phi(\mathbf{r}, t)$. This can be easily used by time-domain SAR focusing algorithms. It is less clear how it will be used in frequency-domain algorithms. The APS information is significant information in its own right, and may well be one of the primary products from a GEO SAR.

### C. Further Design Iterations

This paper describes only an initial system design method. Further iterations should be used to test significant assumptions and to examine system design features that pose important challenges for mission feasibility. Areas for further study are likely to include:

- more realistic atmospheric perturbation scenarios;
- clutter effects representative of the surfaces to be imaged;
- initial quantification of the data handling architecture, e.g., radar PRF selection, data bandwidths, opportunity for onboard presumming of the raw data;
- orbit control and tracking;
- initial system sizing (particularly mass and power budgets).

## IV. Discussion and Conclusion

An initial system design method for GEO radar imaging has been proposed. The method accounts for important system design constraints, and is a general framework that includes all the principal GEO SAR concepts under discussion and all radar wavebands. GEO SAR applications include both surface monitoring, e.g., ground motion and geohazards, and atmosphere (ionospheric electrons and tropospheric moisture). The system design presented here focuses on engineering constraints: user applications have not been discussed in detail but will be a major factor in any complete system design.

Example design solutions are suggested here to illustrate the design method. The solutions depend on the assumed atmospheric properties, as well as other system parameters, and thus should be reviewed based on a range of likely atmospheric conditions for the region and applications of interest.

GEO SAR is versatile in terms of operations, since viewing can be directed anywhere within the field of view at any time. However, imaging performance is best when the azimuthal motion is large. Periods around the two times each day when the azimuthal component is near zero are less useful for imaging. Ionospheric disturbances cycle over a solar day, whereas the orbit repeats on a sidereal day. A GEO orbit will be therefore favorably aligned for imaging a particular region at different solar times through the year. Given the range of potential applications, their differing needs for temporal coverage and resolution, and varying atmospheric constraints, it will be a significant operational challenge to develop the imaging schedule.

Several areas of further work are suggested by this paper. Some of the most important for system design are to extend the range of atmospheric perturbations included (e.g., to include ionospheric scintillations [35]) and to quantify the impact of actual surface properties on imaging. In addition, it is important to assess potential applications that might justify investment in a GEO SAR mission. Finally, a development roadmap is required. This may include technology demonstrators and should mitigate technology risks early on.

Studies so far suggest that GEO SAR has great potential. It could provide radically new data products with temporal resolution, which single LEO satellites cannot match. Its ability to measure ground properties and dynamic atmospheric structure simultaneously is unrivalled, and the GEO viewpoint enables highly versatile imaging modes. It cannot provide complete coverage (water surfaces and other unstable targets are not measurable), however its potential contribution to the global EO system—including complementing LEO SAR—is significant.

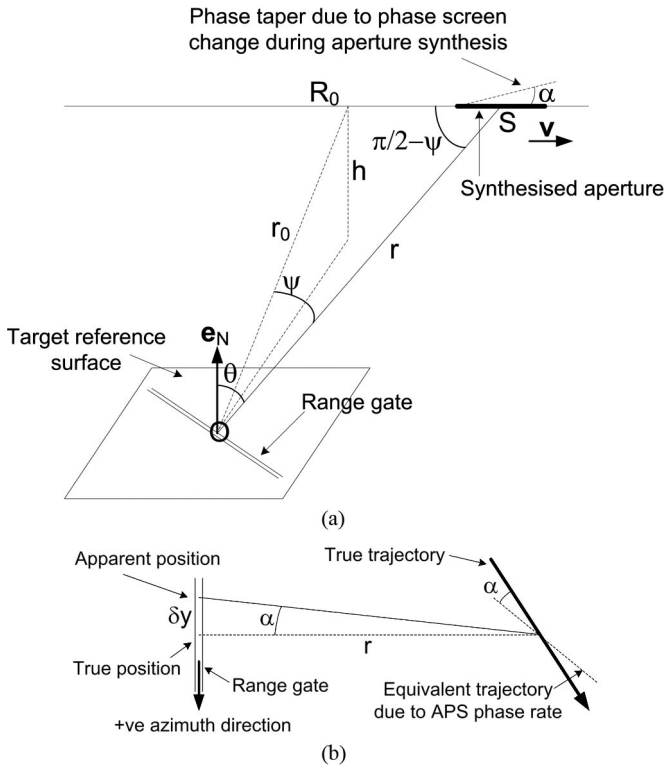


Fig. 9. Azimuth shift due to phase screen change during aperture synthesis. (a) Phase change during aperture synthesis, equivalent to a rotation of the trajectory. (b) Azimuth shift due to effective rotation of satellite trajectory.

## APPENDIX A
## AZIMUTH SHIFT DUE TO APS CHANGE

The azimuth shift due to changes in atmospheric path delay is derived here. It is in principle equivalent to the azimuth shift due to motion of the target in the slant direction. Assume the rate of change of the phase screen (One-way, zenith) over the target is $\dot{\phi}$ during integration time $t$. At wavelength $\lambda$, this phase change can be converted to an equivalent change in (one-way) optical path length $\delta l$ [(26), allowing for the local incidence angle $\theta$]. This extra path increases steadily during integration time $t$, and has the same effect as a slight rotation of the satellite trajectory by an angle $\alpha = \delta l / vt$ (Fig. 9) in the plane of the satellite velocity and slant range. Since SAR focusing assumes the actual trajectory and not the rotated trajectory, points appear to be displaced in azimuth opposite to the satellite velocity by a distance $\delta y$, which subtends the angle $\alpha$. The geometrical factor $\mathbf{e}_2 \cdot \mathbf{e}_a$ (derived below) accounts for velocity in general not being parallel to the range gate. Thus

$$\delta l = \dot{\phi} t \frac{\lambda}{2\pi} \frac{1}{\cos\theta} \tag{26}$$

$$\delta y = -\frac{r\alpha}{\mathbf{e}_2 \cdot \mathbf{e}_a} = -\frac{r\delta l}{vt(\mathbf{e}_2 \cdot \mathbf{e}_a)} = \frac{r\dot{\phi}\lambda}{2\pi v \cos\theta (\mathbf{e}_2 \cdot \mathbf{e}_a)}. \tag{27}$$

The geometry of the azimuth shift due to changes in the APS is defined by three vectors:

- the velocity vector (unit vector $\mathbf{e}_v$);
- the slant range vector from target to satellite (unit vector $\mathbf{e}_r$);

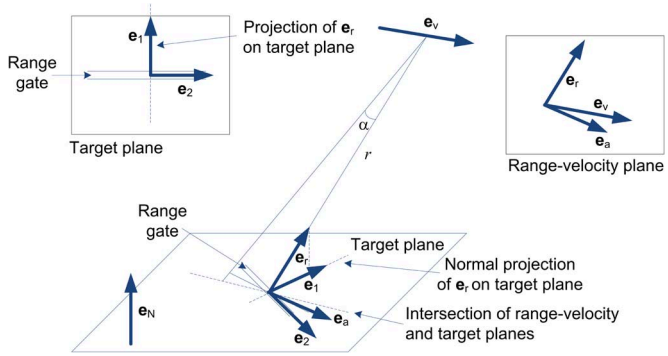


Fig. 10. Geometry of APS influence on azimuth shift.

- the vector normal to the target plane (unit vector $\mathbf{e}_N$).

The rotation due to the changing phase delay occurs in the velocity-range plane; the azimuth offset occurs in the target plane. Vectors defining orthogonal coordinate directions in either the velocity-range or target planes are:

- unit vector $\mathbf{e}_a$ in the velocity-range plane, normal to $\mathbf{e}_r$;
- unit vector $\mathbf{e}_1$ in the target plane, parallel to the projection of $\mathbf{e}_r$ onto the target plane;
- unit vector $\mathbf{e}_2$ in the target plane, perpendicular to $\mathbf{e}_1$ and parallel to the azimuth direction in the range gates.

Fig. 10 shows the geometry assumed. These vectors are defined using the following relationships.

$$\mathbf{e}_a = a\left[\mathbf{e}_v - \mathbf{e}_r(\mathbf{e}_v \cdot \mathbf{e}_r)\right], \quad a = \frac{1}{\sqrt{1-(\mathbf{e}_v \cdot \mathbf{e}_r)^2}}$$

$$\mathbf{e}_1 = b\left[\mathbf{e}_r - \mathbf{e}_N(\mathbf{e}_r \cdot \mathbf{e}_N)\right], \quad b = \frac{1}{\sqrt{1-(\mathbf{e}_r \cdot \mathbf{e}_N)^2}}$$

$$\mathbf{e}_2 = \mathbf{e}_1 \times \mathbf{e}_N.$$

The azimuth offset within the range gate is such that when projected onto $\mathbf{e}_a$ it has magnitude $r\alpha$ (slant range multiplied by the rotation angle).

$$r\alpha = -\delta y \mathbf{e}_2 \cdot \mathbf{e}_a, \qquad \delta y = -\frac{r\alpha}{\mathbf{e}_2 \cdot \mathbf{e}_a}. \tag{28}$$

## APPENDIX B
## AVERAGING GAIN LIMIT

The limit for small phase intervals $\omega\Delta t$ can be approximated using a Taylor expansion around $t_0$ ignoring terms higher than second order. Linear time dependence causes an azimuth shift and thus is ignored as a source of defocusing (we write $\theta = \omega\delta t$ for the phase interval variable, and $\Delta\theta = \omega\Delta t$).

$$\phi(t) = a_0 \sin(\omega t + \psi_0) \tag{29}$$
$$= \phi(t_0) + \dot{\phi}(t_0)(t-t_0) + \ddot{\phi}(t_0)\frac{(t-t_0)^2}{2} + \ldots$$

$$\phi_1(t_0+\delta t) = \phi(t_0) + \ddot{\phi}(t_0)\frac{\delta t^2}{2} = \phi(t_0)\left(1 - \frac{\theta^2}{2}\right). \tag{30}$$

The average value of $(\theta^2/2)$ over the interval $(-\Delta\theta/2, \Delta\theta/2)$ represents a phase offset that can be subtracted so that

the remainder has zero mean

$$\overline{\theta^2} = \frac{1}{\Delta\theta} \int_{-\Delta\theta/2}^{\frac{\Delta\theta}{2}} \theta^2 \, d\theta = \frac{\Delta\theta^2}{12}. \tag{31}$$

To second order, the nonlinear part of the phase perturbation due to a sinusoidal phase variation can be written as a constant part $\phi_{1a}$ and a variable part $\phi_{1b}$ with zero mean

$$\phi_1(t_0 + \delta t) = \phi(t_0)\left(1 - \frac{\theta^2}{2}\right) = \phi_{1a} + \phi_{1b}$$
$$\phi_{1b} = \phi(t_0)\left(\frac{\Delta\theta^2}{24} - \frac{\theta^2}{2}\right). \tag{32}$$

The variable part causes loss of phasor amplitude, which can be quantified (the constant part is only a phase offset)

$$g = \frac{1}{\Delta\theta} \int_{-\Delta\theta/2}^{\frac{\Delta\theta}{2}} e^{i(\phi_{1a}+\phi_{1b})} \, d\theta \tag{33}$$
$$= e^{i\phi_{1a}} \times \frac{1}{\Delta\theta} \int_{-\Delta\theta/2}^{\frac{\Delta\theta}{2}} e^{i\phi_{1b}} \, d\theta = g_1 \times g_2$$
$$g_2 = \frac{1}{\Delta\theta} \int_{-\Delta\theta/2}^{\frac{\Delta\theta}{2}} e^{i\phi_{1b}} \, d\theta. \tag{34}$$

By symmetry the imaginary part of $g_2$ is zero, and thus, only the real part is required. For small $x = a_0(\Delta\theta^2/12)$, $\cos x$ can be usefully expanded as $(1 - x^2/2)$

$$g_2 = \frac{1}{\Delta\theta} \int_{-\Delta\theta/2}^{\frac{\Delta\theta}{2}} \cos\left(\phi(t_0)\left[\frac{\Delta\theta^2}{24} - \frac{\theta^2}{2}\right]\right) d\theta \tag{35}$$
$$\simeq 1 - \frac{\sin^2(\omega t_0 + \psi_0)}{10}\left(\frac{a_0\Delta\theta^2}{12}\right)^2. \tag{36}$$

Contours of constant gain are thus lines with $a_0\Delta\theta^2 = c$ (constant), or $\Delta\theta = c/\sqrt{a_0}$ (14).

## ACKNOWLEDGMENT

Discussions with colleagues, particularly D. Hall (EADS Astrium), Prof. F. Rocca and Prof. A. Monti-Guarnieri (Politecnico di Milano), Prof. M. Rycroft, and postgraduate students at Cranfield University, have contributed significantly to the research. The author would like to thank the Royal Society Wolfson Award and EPSRC Grant EP/H003304/1. The reviewers' thoughtful and constructive comments are much appreciated.

## REFERENCES

[1] K. Tomiyasu and J. L. Pacelli, "Synthetic aperture radar imaging from an inclined geosynchronous orbit," *IEEE Trans. Geosci. Remote Sens.*, vol. GE-21, no. 3, pp. 324–329, Jul. 1983.

[2] S. Madsen, W. Edelstein, L. DiDomenico, and J. LaBrecque, "A geosynchronous synthetic aperture radar; for tectonic mapping, disaster management and measurements of vegetation and soil moisture," in *Proc. IEEE IGARS*, 2001, vol. I, pp. 447–449.

[3] E. Im, S. L. Durden, Y. Rahmat-Samii, M. Lou, and J. Huang, "Conceptual design of a geostationary radar for monitoring hurricanes," presented at the Earth Sci. Technol. Conf., Univ. of Maryland, College Park, MD, USA, Jun. 24–26, 2003.

[4] W. Edelstein, S. Madsen, A. Moussessian, and C. Chen, "Concepts and technologies for synthetic aperture radar from MEO and geosynchronous orbits," in *Enabling Sensor and Platform Technologies for Spaceborne Remote Sensing*, vol. 5659, G. Komar, J. Wang, and T. Kimura, Eds. Bellingham, WA, USA: SPIE, 2005, pp. 195–203.

[5] C. Prati, F. Rocca, D. Giancola, and A. Monti Guarnieri, "Passive geosynchronous SAR system reusing backscattered digital audio broadcasting signals," *IEEE Trans. Geosci. Remote Sens.*, vol. 36, no. 6, pp. 1973–1976, Nov. 1998.

[6] S. Hobbs, "GeoSAR: Summary of the group design project, MSc in astronautics and space engineering 2005/06," Cranfield University, Bedford, U.K., College of Aeronautics Rep. 0509, Aug. 2006.

[7] D. Bruno and S. E. Hobbs, "Radar imaging from geosynchronous orbit: Temporal decorrelation aspects," *IEEE Trans. Geosci. Remote Sens.*, vol. 48, no. 7, pp. 2924–2929, Jul. 2010.

[8] S. Hobbs *et al.*, "Simulation of geosynchronous radar and atmospheric phase compensation constraints," in *Proc. IET Int. Radar Conf.*, Xi'an, China, 2013, pp. 1–6.

[9] A. Monti Guarnieri, F. Rocca, and A. B. Ibars, "Impact of atmospheric water vapor on the design of a Ku band geosynchronous SAR system," in *Proc. IEEE IGARSS*, Cape Town, Republic of South Africa, Jul. 12–17, 2009, vol. 2, pp. II-945–II-948.

[10] A. Monti Guarnieri *et al.*, "Design of a geosynchronous SAR system for water-vapour maps and deformation estimation," presented at the Fringe, Paris, France, 2011, ESA SP-697.

[11] A. Monti Guarnieri *et al.*, "Wide coverage, fine resolution, geosynchronous SAR for atmospheric and terrain observations," presented at the *Living Planet Symp.*, paper no. ESA SP-722, 2013.

[12] J. Ruiz Rodon, A. Broquetas, E. Makhoul, A. Monti Guarnieri, and F. Rocca, "Results on spatio-temporal atmospheric phase screen retrieval from long-term GEOSAR acquisition," presented at the Proc. IEEE IGARSS, Munich, Germany, Jul. 22–27, 2012, pp. 3289–3292.

[13] J. Ruiz Rodon, A. Broquetas, A. Monti Guarnieri, and F. Rocca, "Geosynchronous SAR focussing with atmospheric phase screen retrieval and compensation," *IEEE Trans. Geosci. Remote Sens.*, vol. 51, no. 8, pp. 4397–4404, Aug. 2013.

[14] M. Bao, Y. Liao, Z. J. Tian, M. D. Xing, and Y. C. Li, "Imaging algorithm for GEO SAR based on series reversion," in *Proc. IEEE CIE Int. Conf. Radar*, Chengdu, China, Oct. 24–27, 2011, vol. 2, pp. 1493–1496.

[15] X. Dong, Y. Gao, C. Hu, T. Zeng, and C. Dong, "Effects of Earth rotation on GEO SAR characteristics analysis," in *Proc. IEEE CIE Int. Conf. Radar*, Chengdu, China, Oct. 24–27, 2011, vol. 1, pp. 34–37.

[16] C. Hu, T. Long, T. Zeng, F. Liu, and Z. Liu, "The accurate focusing and resolution analysis method in geosynchronous SAR," *IEEE Trans. Geosci. Remote Sens.*, vol. 49, no. 10, pp. 3548–3563, Oct. 2011.

[17] C. Hu, Z. Liu, and T. Long, "An improved CS algorithm based on the curved trajectory in geosynchronous SAR," *IEEE J. Sel. Topics Appl. Earth Observ. Remote Sens.*, vol. 5, no. 3, pp. 795–808, Jun. 2012.

[18] X. Dong, C. Hu, and T. Zeng, "Antenna area constraint in GEO SAR," in *Proc. IET Int. Radar Conf.*, Xi'an, China, Apr. 14–16, 2013, pp. 1–4.

[19] L. Kou, M. Xiang, X. Wang, and M. Zhu, "Tropospheric imaging on L-band geosynchronous circular SAR imaging," *IET Radar, Sonar Navigat.*, vol. 7, no. 6, pp. 683–701, Jul. 2013.

[20] C. Hu, X. Li, T. Long, and Y. Gao, "GEO SAR interferometry: Theory and feasibility study," in *Proc. IET Int. Radar Conf.*, Xi'an, China, Apr. 14–16, 2013, pp. 1–5.

[21] R. S. Lawrence, C. G. Little, and H. J. Chivers, "A survey of ionospheric effects upon earth-space radio propagation," *Proc. IEEE*, vol. 52, no. 1, pp. 4–27, Jan. 1964.

[22] S. Quegan and J. Lamont, "Ionospheric and tropospheric effects on synthetic aperture radar performance," *Int. J. Remote Sens.*, vol. 7, no. 4, pp. 525–539, 1986.

[23] Z.-W. Xu, J. Wu, and Z.-S. Wu, "A survey of ionospheric effects on space-based radar," *Waves Random Media*, vol. 14, no. 2, pp. S189–S273, 2004.

[24] Y. Otsuka *et al.*, "GPS observations of medium-scale traveling ionospheric disturbances over europe," *Annales Geophys.*, vol. 31, no. 2, pp. 163–172, 2013.

[25] Z. Katamzi, N. Smith, C. Mitchell, P. Spalla, and M. Materassi, "Statistical analysis of travelling ionospheric disturbances using TEC observations from geostationay satellites," *J. Atmosp. Solar-Terrestrial Phys.*, vol. 74, pp. 64–80, 2012.

[26] M. Hernandez-Pajares, J. Juan, J. Sanz, and A. Aragon-Angel, "Propagation of medium scale traveling ionospheric disturbances at different latitudes and solar cycle conditions," *Radio Sci.*, vol. 47, no. 6, pp. 1–22, 2012.
[27] R. Hanssen, *Radar Interferometry, Data Interpretation and Error Analysis*. Norwell, MA, USA: Kluwer, 2001.
[28] B. Parkinson and J. Spilker, Eds., *Global Positioning System: Theory and Applications*, vol. I. Reston, VA, USA: AIAA, 1996, ser. Progress in Astronautics and Aeronautics, vol. 163.
[29] *Station-Keeping in Longitude of Geostationary Satellites in the Fixed-Satellite Service*, Int. Telecommun. Union Std. ITU-R S.484-3, 1992, 2000.
[30] D. Vallado, *Fundamentals of Astrodynamics and Applications*, 4th ed. Portland, OR, USA: Microcosm Press, 2013.
[31] P. Fortescue, J. Stark, and G. Swinerd, *Spacecraft Systems Engineering*, 4th ed. New York, NY, USA: Wiley, 2011.
[32] J. Wertz, D. F. Everett, and J. J. Puschell, *Space Mission Engineering: The New SMAD*. Portland, OR, USA: Microcosm Press, 2011, ser. Space Technology Library.
[33] W. Rees, *Physical Principles of Remote Sensing*, 3rd ed. Cambridge, U.K.: Cambridge Univ. Press, 2013.
[34] J. Ruiz Rodon, A. Broquetas, A. Monti Guarnieri, and F. Rocca, "A ku-band geosynchronous synthetic aperture radar mission analysis with medium transmitted power and medium-sized antenna," in *Proc. IEEE IGARSS*, Vancouver, BC, Canada, Jul. 24–29, 2011, pp. 2456–2459, no. WE2.TO4.3.
[35] N. C. Rogers, S. Quegan, J. S. Kim, and K. P. Papathanassiou, "Impacts of ionospheric scintillation on the BIOMASS P-band satellite SAR," *IEEE Trans. Geosci. Remote Sens.*, vol. 52, no. 3, pp. 1856–1868, Mar. 2014.
[36] D. Belcher, "Theoretical limits on SAR imposed by the ionosphere," *IET Radar, Sonar Navigat.*, vol. 2, no. 6, pp. 435–448, 2008.

**Stephen Hobbs** received the B.S. degree in mathematics and physics from Trinity College, Cambridge University, Cambridge, U.K., in 1980, and the Ph.D. degree in ecological physics from Cranfield Institute of Technology, Bedford, U.K. for work on kite anemometry.

Since 2004, he has been the Director with the Cranfield Space Research Centre, Cranfield University, Bedford, U.K. Since 1992, he has been involved with the School of Engineering's space engineering research and teaching. Prior to that, he worked on radar remote sensing and instrumentation in Cranfield's Ecological Physics Research Group and College of Aeronautics. In 2001, he was seconded to Astrium U.K. Ltd., Hertfordshire, U.K., to work on the European Space Agency's GAIA mission and a small radar satellite. His current research includes sustainability of space activities and measurement physics aspects of geosynchronous radar remote sensing.

Dr. Hobbs is a member of the Royal Meteorological Society, the Institute of Physics, and the Remote Sensing and Photogrammetry Society (for which he is convenor of the Synthetic Aperture Radar Special Interest Group).

**Cathryn Mitchell** received the B.Sc. and Ph.D. degrees in physics from the University of Wales Aberystwyth, Dyfed, U.K.

In 1999, she joined the University of Bath, Bath, U.K. Her research interests include the effects of atmospheric scintillation and multipath propagation on GPS navigation signals, tomography (medical and geophysical), and the influence of the Sun upon the magnetosphere and ionosphere. Her research interests include radio propagation, signal processing, and the inversion of multidirectional signals to reveal interesting information about the natural world.

**Biagio Forte** received the B.S. degree in physics from the University of Trieste, Trieste, Italy, and the Ph.D. degree in geophysics from Karl-Franzens University of Graz, Graz, Austria.

In 2012, he joined the University of Bath, Bath, U.K., as a Prize Fellow in Space Weather. His fellowship aims at devising countermeasures to mitigate space weather vulnerabilities affecting satellite navigation, for example, in support to civil aviation. His research interests include physics and chemistry of the upper ionized atmosphere, propagation of electromagnetic waves, RF engineering, space weather phenomena and their effects, remote sensing of atmospheres, and low-frequency radio astronomy.

**Rachel Holley** (M'12) received the MESci degree in earth sciences from the University College, Oxford University, Oxford, U.K., in 2004, and the Ph.D. degree from the University of Reading, Berkshire, U.K., for work on mitigation of atmospheric path delays in interferometric synthetic aperture radar (InSAR).

Since 2009, she has been with the InSAR Surveying Department, NPA Satellite Mapping, Kent, U.K. As a Senior Technical Lead within the department, she has worked on a wide variety of commercial, publicly funded and internal research projects. She has particular experience using Persistent Scatterer Interferometry and differential interferometric SAR techniques in challenging terrain for natural hazard applications, mining, oil, and gas field deformation and geothermal areas.

Dr. Holley is a member of IEEE Geoscience and Remote Sensing Society, the European Geoscience Union, the Remote Sensing and Photogrammetry Society, and the Geological Remote Sensing Group.

**Boris Snapir** received the M.Sc. degree in astronautics and space engineering.

He is a Researcher with Cranfield University's Space Research Centre, Bedford, U.K., studying radar remote sensing for applications in agriculture and meteorology. He is developing methods of data assimilation to couple models of surface processes, such as soil moisture with Earth observation data, and is also applying these techniques to aspects of the geosynchronous synthetic aperture radar mission design.

**Philip Whittaker** received the Ph.D. degree from the Surrey Space Centre, University of Surrey, Surrey, U.K., investigating payload architectures for in-orbit monitoring of the RF spectrum.

He is a Senior RF Systems Engineer with Surrey Satellite Technology Ltd. (SSTL), Guildford, U.K. and a Technical Lead for synthetic aperture radar (SAR) activities. Since 2001 he has worked with SSTL on telemetry, telecommand and control subsystems and RF payloads for navigation and remote sensing. For the past three years, he was responsible for developing mission and payload concepts for low-cost spaceborne SAR solutions.

2014-05-08

# System design for geosynchronous synthetic aperture radar missions

Hobbs, Stephen

IEEE

Hobbs S, Mitchell C, Forte B, et al., (2014) System design for geosynchronous synthetic aperture radar missions. IEEE Transactions on Geoscience and Remote sensing, Volume 52, Issue 12, December 2014, pp. 7750-7763

http://doi.org/10.1109/TGRS.2014.2318171